**RESEARCH PAPER**

# Large-Scale Fatigue Testing Based on the Rotating Beam Method

**M. Isakov[1]** · **O. Rantalainen[1]** · **T. Saarinen[2]** · **A. Lehtovaara[1]**

**Abstract**

A large-scale fatigue testing machine based on the rotating beam method in a four-point bending configuration was designed and built. With the device, high-strength metal specimens with a 32-mm gauge diameter and a 100-mm gauge length can be tested at a cyclic frequency of up to 48 Hz. In this work, particular attention was paid to evaluating the spatial and temporal uniformity of the loading within the large specimen; methods for quantitative evaluation of these effects were developed. The developed test methodology allows for the fatigue testing of specimens with size, microstructure, and surface conditions that are similar to actual machine parts.

**Keywords** Fatigue testing · Rotating beam · Rotating bending · Size effect

## Introduction

It is well known that material fatigue involves a size effect, i.e., the physical size of the loaded solid affects its fatigue properties. This introduces a notable challenge in the design against fatigue, because in most cases the available material data are based on laboratory tests where the specimens are considerably smaller than the actual machine components and structures subjected to cyclic loading. Thus, in order to account for the size effects on the fatigue properties and achieve the required reliability of the structure, the laboratory results have to be scaled with some appropriate means [1]. If sufficient reliability cannot be reached in the predictions, then one is forced to use time-consuming and expensive full-scale tests and/or use very conservative safety margins in the design.

Based on the current understanding [1], the size effect in fatigue can be considered to involve three categories: the statistical, geometrical, and technological size effects. The *statistical size effect* [2–4] relates to the fact that the probability of the existence of a detrimental defect in a given solid piece increases as its volume increases. The *geometrical size effect* [5–8], in turn, refers to the influence of the physical dimensions of geometrical discontinuities, such as notches, on the fatigue behavior. Even if there is no difference in the notch shape and in the peak stress at the notch root, a smaller notch will in general result in a higher fatigue limit than a larger notch due to the differences in the size of the notch stress field and in the growth mechanisms of short and long cracks. The *technological size effect* arises because production processes, such as heat treatments and machining operations, generally result in a different material state depending on the size of the produced component. For example, in quenching, the resulting microstructure and its homogeneity depends on the effective cooling rate within the solid and hence on the size of the quenched component.

The current study is focused on developing experimental capabilities to study material fatigue with large-sized specimens. The study is motivated by the following aspects: Firstly, as noted by Zhu et al. in a recent review [1], the technological size effect has received less attention in the literature than the two other categories discussed above. The technological size effect tends to be case-specific by nature, and it is difficult to draw general theories with a good predictive capability. Secondly, the three categories of the size effect are inherently linked. For example, the probability distribution of detrimental defects in the material, which belongs to the category of statistical size effects, may depend on the production process, which in turn relates to the technological size effect. Similar reasoning applies to geometrical features, such as notches.

✉ M. Isakov
matti.isakov@tuni.fi

[1] Materials Science and Environmental Engineering, Tampere University, Korkeakoulunkatu 6, 33720 Tampere, Finland

[2] Sandvik Mining and Construction Oy, Pihtisulunkatu 9, P.O.B. 100, 33311 Tampere, Finland

Based on the discussion above, there are several reasons supporting the fatigue testing of large specimens in addition to normal small-scale laboratory testing. However, the challenges in such an approach are also evident: when a fatigue test is scaled up, such as in [9], the size and mass of the test machine and its moving parts increase rapidly. This brings about challenges in the test procedures and may notably limit the maximum loading frequency due to the inertia of the moving parts and high energy demand. On the other hand, if the problem is approached from the application side, i.e., if a replica or a somewhat scaled-down version of the actual component is used in a custom-made rig, such as in [10–13], then the obtained results tend to be case-specific and it is challenging to draw general conclusions. Therefore, fatigue testing with large test specimens that are comparable in geometry to small (standardized) specimen types is not a straightforward or small undertaking. This can at least partly explain the fact that, to the authors' knowledge, this type of testing is relatively seldom reported in the open literature. Recent accounts involve up-scaled rotating bending test setups [14, 15] as well as axial loading setups based on either hydraulic actuation [9] or structural resonance [16]. These test setups differ from each other considerably, which indicates that the best practices are not yet fully established and there is room for further contributions in the field.

In this paper, the above-mentioned challenges are approached with a large-scale rotating beam (bending) fatigue machine (RBFM). The current device allows for the cyclic testing of high-strength metal specimens with a gauge diameter of 32 mm and a gauge length of 100 mm at a loading frequency of up to 48 Hz. The developed test device facilitates efficient SN-curve and fatigue limit measurement using specimens that have the size, microstructure, and surface conditions similar to the ones in actual machine components. The main purpose of the current contribution is to highlight and discuss that even in a relatively simple concept presented here, there are critical points related to designing the device, developing the analytical methods, and carrying out materials testing at this size scale. In the authors' opinion, these topics have not been thoroughly discussed in the open literature until now.

## Design of the Test Device

In the following, the main design aspects of the test device are described. The primary design goal was to facilitate efficient fatigue testing of large-scale metallic specimens with well-defined imposed loading, i.e., to design a "materials test" and to try to avoid the non-generalities related to a "structural test." Furthermore, for the determination of the fatigue limit, a high enough test frequency (millions of cycles per day) should be reached, while the size and cost

of the test device should be kept reasonable. The design requirement for the specimen loading amplitude was set to 1000 MPa, i.e., to a load level sufficient for high-cycle fatigue studies of high-strength metals. Based on these somewhat conflicting requirements, the classical rotating beam (bending) method was selected, since it allows for relatively straightforward specimen design and manufacturing, well-defined loading on the specimen, a high testing frequency with low energy demand, and in general a simple structure for the device (compared, e.g., to up-scaling a hydraulic fatigue testing machine or setting up a resonance-based loading system). As illustrated by Fig. 1, in the rotating beam method, cyclic loading is achieved by rotating a cylindrical specimen, which is simultaneously loaded in static bending. The obvious drawback of this method is that only the surface of the specimen is loaded by the maximum stress amplitude while the specimen centerline experiences zero loading. Even though this drawback can be overcome in statistical analysis by using, e.g., volume-based weakest link methods [4], some technological aspects, such as microstructural differences between the surface and interior, might be overlooked. However, this drawback was deemed acceptable since the main purpose of the test device is to study various surface-related phenomena in large-scale specimens and by the fact that fatigue failure commonly originates on the surface of the component. Furthermore, four-point bending was selected to obtain a constant bending moment over the specimen gauge length (Fig. 1) and to thus increase the volume of the cyclically loaded material. The second obvious drawback of the rotating beam method is that the mean load cannot be applied on the specimen. In the presented
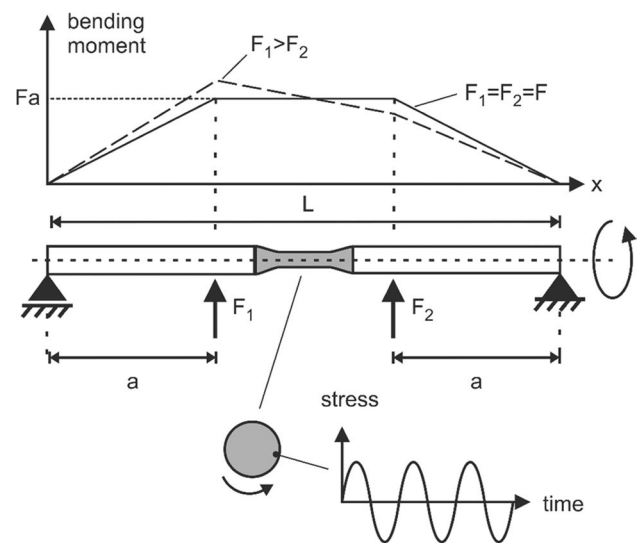


**Fig. 1** Schematic illustration of the rotating beam test method. The presented axial bending moment distribution shows the cases of uniform and non-uniform bending loads ($F_1$, $F_2$), the latter of which will be considered in detail in the analysis of specimen loading

study, this drawback was accepted due to the beneficial features mentioned above.
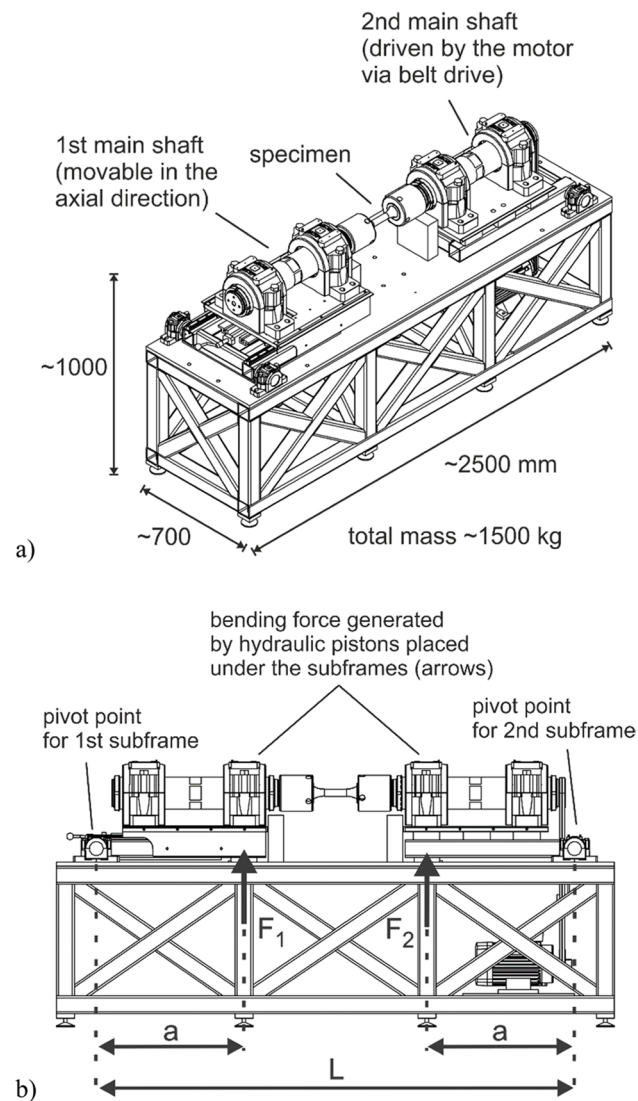


**Fig. 2 a** Overview of the designed large-scale rotating beam fatigue machine and (**b**) sideview with the main support and loading points highlighted. The protective shields placed around the rotating parts during operation are not shown

After the operating principle of the test device was agreed on, detailed design work was carried out by following the general principles of systematic machine design [17, 18]. In the following, the main aspects of the design are presented. Figure 2 shows the general structure of the developed test device, while Table 1 lists the main dimensions of the device, some of which are used later in conjunction with the load analysis. The main principle followed in the design was to benefit from the simplicity offered by the chosen main concept (rotating beam method). For this reason, the two shafts attached to the specimen are supported by subframes, which have pivot points at their ends. Static bending loading is generated with two manually operated hydraulic pistons placed under the middle support points of the subframes. The bending forces are measured with load cells placed between the subframes and the hydraulic pistons. The rotation of the shaft is facilitated with an electric motor and a belt drive. This approach fulfills the requirements set for the test device—i.e., the capability to measure the SN-curve and fatigue limit—but at the same time keeps the level of diagnostics and control requirements simple. Furthermore, in terms of structural vibrations, the main source of excitation is the rotation of the main shaft, which can be accurately controlled by adjusting the rotating speed of the electric motor using a frequency convertor.

The most challenging part of the design process comprised the main shafts and the specimen gripping. This part of the design involved finding a compromise between several partly conflicting criteria, as illustrated in Fig. 3. As noted above, the main design goal was to obtain a high cyclic loading frequency on a large specimen. This introduced an immediate challenge in finding suitable bearings for large-diameter shafts. The challenge was solved by selecting the largest off-the-shelf self-aligning ball bearings, which could sustain a high rotating speed (~ 3000 RPM) under relatively low transverse loading, allow for grease lubrication (for overall simplicity), and offer an almost infinite lifetime under the desired operating conditions. The selection of the bearing then set the maximum shaft diameter and therefore also the upper limit for the specimen grip section diameter. This, in turn, largely determined the maximum specimen gauge section diameter via the requirement that

**Table 1** Numerical values for the main dimensions of the test device

| Dimension | Symbol | Value (mm) |
|---|---|---|
| Distance between the main shaft pivot points, i.e., length of the bending beam (Figs. 1 and 2) | L | 2146 |
| Distance between the main shaft pivot point and the bending load application point (Figs. 1 and 2) | a | 662 |
| Vertical offset between the main shaft centerline and the main shaft pivot point (Fig. 5) | b | 249 |
| Distance between the main shaft bearings (Fig. 5) | c | 450 |
| Specimen gauge diameter | - | 32 |
| Specimen gauge length | $L_0$ | 100 |
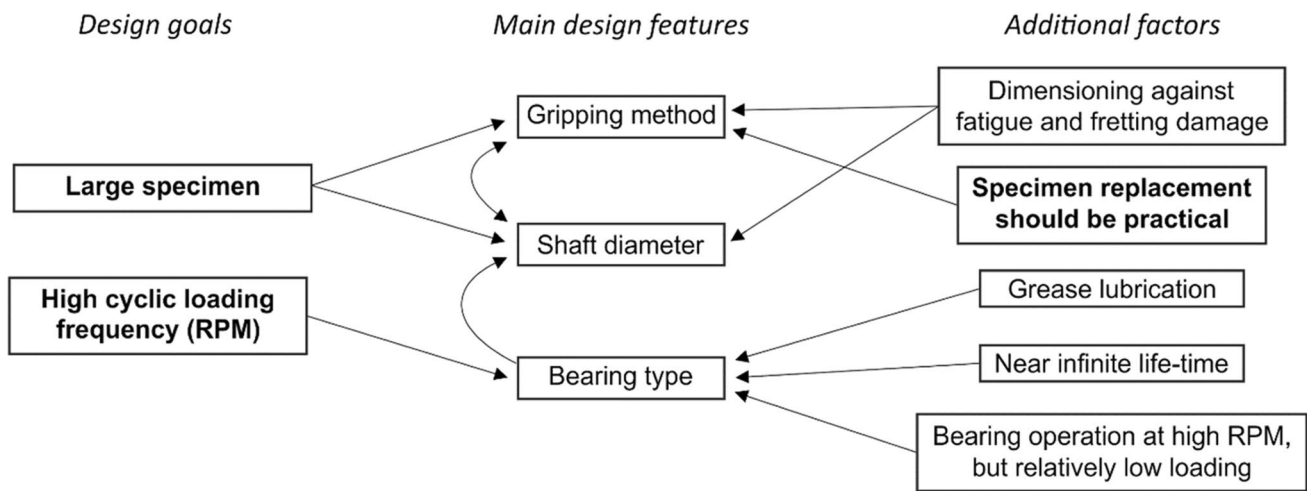
**Fig. 3** Schematic presentation of the main aspects considered in the design process of the main shaft
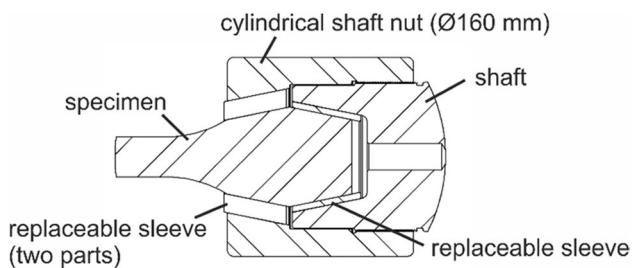


**Fig. 4** A cross-sectional view on the specimen gripping

the probability for fatigue failure outside the gauge section should be minimized (here the recommendations of the ISO1143 standard [19] were followed in the applicable parts).

The main requirements for the specimen gripping were the following: 1) the joint between the specimen and the shaft must transfer the bending loading without interfering with the stress state within the specimen gauge section; 2) the joint must withstand a large amount of loading cycles with minimal damage to the specimen and near zero damage to the test device; 3) the joint should preferably be self-aligning, thus facilitating high RPM operation with minimal adjustment between specimens; 4) the specimen should preferably be rotationally symmetric, i.e., its manufacturing should involve only turning and related machining operations; and 5) the specimen replacement should be practical, i.e., accomplished by one operator within a couple of hours and using hand-held tools.

After considering several options, including a lock sleeve, a threaded specimen, and a specimen with a large dowel pin, the concept based on a conical joint and a large shaft nut shown in Fig. 4 was selected. The conical joint meets the requirements for self-alignment and specimen symmetry, but on the other hand necessitates the possibility to move one of the shafts in the axial direction so that the specimen can be replaced. Moreover, it is well known that conical joints are vulnerable to fretting, i.e., contact surface damage with possibly catastrophic consequences resulting from tangential frictional forces and micrometer-scale reciprocating slip between the contacting surfaces [20–22]. In order to minimize fretting, finite element method analysis of the joint was carried out during the design process to determine the optimal geometry and specifications for the tightening torque of the shaft nut. Furthermore, the replaceable sleeves shown in Fig. 4 were added to the interface. Based on the experience gained by running the device, it can be concluded that even though the replaceable sleeves somewhat add to the complexity of the joint (mainly slowing down specimen replacement), they are necessary for the long-term durability of the device; fretting damage does gradually appear on the specimen/sleeve interface, but it is absent on the sleeve/shaft interface. To summarize, in the final joint the bending moment (~ 1… 5 kNm) is transferred between the shaft and the specimen by the shaft nut, i.e., through the shaft/nut thread. The tightening torque (around 1500 Nm) applied to the nut generates an axial force (~ 100 kN) that provides the necessary normal pressure for the interfaces and, most importantly, decreases the cyclic loading on the thread to an acceptable level. In order to meet the requirement for the practical usability of the test device, the subframe supporting one of the main shafts incorporates rails that allow for axial movement of the shaft during specimen replacement with a hand-operated spindle. In addition, manually operated hydraulic tools were built for the tightening and loosening of the shaft nut. With these tools, an experienced operator is in practice able to replace the specimen after a test and prepare for a new test in roughly

one working day, which is, although on the lengthy side, still acceptable for the intended purpose of the test device.

It should be noted that the device does not have a brake on the main shaft; this was considered during the design phase and it was concluded that for effective operation—i.e., rapidly stopping the two shafts with a combined weight well over 100 kg and rotating up to 2800 RPM—the necessary modifications would make the resulting structure notably more complex than the current one. Instead, operator safety is ensured by placing protective shields around the rotating parts (not shown in Fig. 2) and setting up the device controls so that the operator does not have to be in the immediate vicinity of the device while it is running.

## Instrumentation and Device Characteristics

As noted above, the general simplicity of the rotating beam method allows for rather simple diagnostics and control during operation. In the developed test setup, the following measurement data are acquired and processed real-time by the *imc Cronos PL2* data acquisition device running at 10 kHz: the bending forces measured by two load cells (*KAM,* 100 kN) placed between the hydraulic pistons and the subframes, shaft rotation measured with an inductive sensor (*HIGHLY*), lateral acceleration measured with a piezo-electric sensor (*Kistler*, $\pm 50$ g) placed on top of one of the bearing housings, the temperature of the electric motor (K-type thermocouple attached to the motor casing), and specimen strain measured with a *Kraus Messtechnik T1-PCM-IND* wireless strain gauge telemetry system. The wireless system is based on a small inductively powered transmitter, which is mounted to one of the shaft nuts. Both the power to the transmitter and the pulse code-modulated (PCM) data signal from the transmitter are transferred wirelessly by a system consisting of an induction winding (copper wire) coiled around the shaft nut and a pickup/powerhead unit fixed to the machine frame. The PCM signal is fed to the rest of the data acquisition system by a decoder unit. Two 5-mm gauge length strain gauges are attached in the axial direction at the center of the specimen gauge section (on opposite sides) and connected to the transmitter in a half-bridge configuration (bending strain measurement).

The simple operating principle allows for simple control logic. During the test, a frequency converter drives the electric motor at a pre-set RPM and the data acquisition device monitors the measurement channels. When one or more of the input channels violate their pre-set limits (which were determined based on initial test runs), the data acquisition device cuts the control signal to the frequency converter, which immediately cuts power to the motor, thus facilitating fully automated over-night operation of the machine. Since there is no brake in the system, the shaft continues rotating for around one minute when the power is switched off at maximum rotating speed (48 Hz). In practice, it was noticed that the most common trigger event is the propagation of the final fracture in the specimen and the resulting rapid decrease in the measured bending force. Therefore, the specimen will most likely fail completely before the main shaft stops rotating. However, when the specimen fails, the tilt angle of the subframes increases slightly (due to the compliance of the loading system), which moves the two specimen surfaces away from each other. This motion is amplified by the offset (*b*) between the subframe pivot point and the main shaft centerline, as illustrated by Fig. 5(a). Thus, the possibility for post-mortem contact damage is notably reduced. This is an important feature of the test, since it allows for the characterization of the fatigue failure surfaces.

The above-mentioned *in-situ* specimen strain measurement was added to verify the specimen strain amplitude during operation. As noted above, there exists an offset (*b*) between the center axis of the main shaft and the subframe pivot point. Due to this offset, axial loading on the main shaft (*N*), when present, generates an additional bending moment with respect to the pivot point of the subframe (Fig. 5(b)), i.e.:

$$Fa - M_t - Nb = 0 \qquad (1)$$

It is evident from equation (1) that this additional bending moment (*Nb*) will result in additional loading on the load cell (*F*) superimposed on the load caused by the actual specimen bending moment (*M_t*). The value of the axial load can be estimated by assuming that it is caused by the friction between the main bearings and their housings. The development of the frictional forces can be understood by referring to Fig. 5(a); due to the offset (*b*), the change in the tilt angle of the subframes is accompanied by an axial motion along the shaft centerline. Since the axially stiff shaft tends to maintain its length, relative motion between the main bearings and their housings takes place, which results in the generation of frictional forces in the axial direction.

Using the free-body diagrams presented by Fig. 5(c), the solution for the axial load can be found:

$$N = 2\mu \frac{M_t}{c} \qquad (2)$$

$$\Rightarrow Fa = M_t\left(1 + 2\mu \frac{b}{c}\right) \qquad (3)$$

where $\mu$ is the coefficient of friction (COF). The numerical values of the geometrical parameters are given in Table 1. For example, using COF = 0.15 (lubricated steel-to-steel contact) results in $Fa = 1.17 M_t$, i.e., there is a 17% difference to the theoretical (frictionless) four-point-bending solution. It is also noted that the sign of the friction effect

**Fig. 5** Illustration of the effects of the offset (*b*) between the main shaft centerline and the pivot point: (**a**) due to the offset, subframe tilting introduces notable axial motion along the shaft centerline; (**b**) due to the offset, the possible axial load (*N*) has to be accounted for in the relationship between the measured bending force (*F*) and specimen bending moment ($M_t$); and (**c**) free body diagrams of the main shaft and the supporting subframe showing the axial frictional forces at the bearings
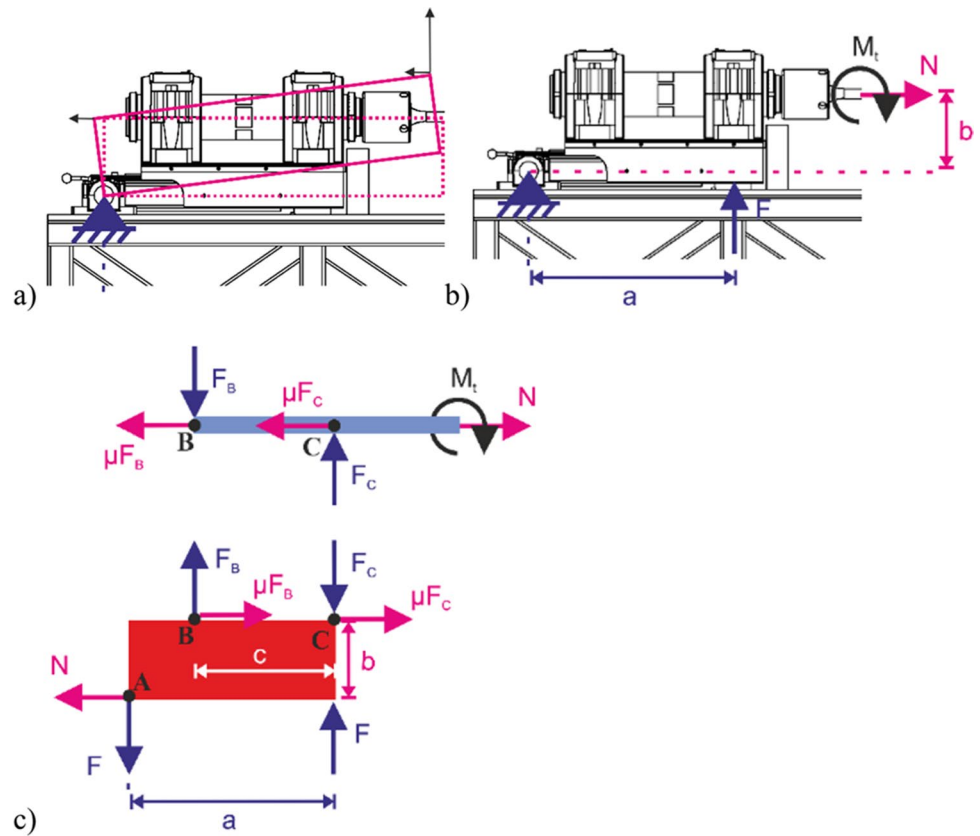


is dependent on whether the bending load is increased or decreased. When the bending load is increased, the friction resists further bending of the main shaft, thus leading to an overestimation of the specimen bending moment; during unloading the opposite happens, i.e., the axial friction maintains an additional bending moment on the specimen despite the decrease of the applied bending force.

Measurements carried out using the wireless strain gauge sensor showed a good correlation with the predictions made above: the effect of axial friction is linear, its maximum value is around ~ 15%, and the effect remains constant during a test run. Therefore, the combination of the *in-situ* strain measurement and the bending force measurement was deemed sufficiently accurate for the specimen stress-state determination.

## Spatial and Temporal Uniformity of the Loading on the Specimen

The large specimen size requires that the uniformity of loading within the specimen gauge section is evaluated. Firstly, a gradient in the stress amplitude may develop along the specimen length if the external loading is not symmetrically applied, as illustrated by Fig. 1. Secondly, geometrical imperfections may be introduced to large specimens during

their manufacture. Based on the authors' experience of running around 70 successful tests with the device presented here, geometrical imperfections of the specimen are common on this size scale, despite the application of state-of-the-art manufacturing methods. Therefore, a thorough analysis of the specimen loading conditions is necessary and will be presented in the following.

In general, the stress amplitude and its longitudinal distribution within the specimen gauge section can be evaluated based on the well-known statics solution for point loads (given that the measured bending loads are scaled appropriately to account for the above-discussed friction effect):

$$\sigma_a\left(\frac{L-L_0}{2} \le x \le \frac{L+L_0}{2}\right) = \left[\Delta F\left(\frac{x}{L}-\frac{1}{2}\right)+\overline{F}\right]\frac{a}{W_0} \quad (4)$$

$$\overline{F} = \frac{1}{2}\left(F_1 + F_2\right) \quad (5)$$

$$\Delta F = F_2 - F_1 \quad (6)$$

In equation (4), *L* and *a* are related to the geometry of the setup, as highlighted by Figs. 1 and 2. The specimen properties, i.e., gauge length and section modulus, are denoted by $L_0$ and $W_0$, respectively. In equations (5) and (6), $F_1$ and $F_2$ denote the bending forces illustrated

by Figs. 1 and 2. As is evident from equations (4) to (6), the stress amplitude within the specimen gauge section is composed of two components; a mean level that is dependent on the mean bending force (equation (5)) and a longitudinal linear field that depends on the difference of the bending forces (equation (6)). It is noted that the bending forces can be, in general, time-dependent. Therefore, one needs to consider both the spatial variation of the stress amplitude (given by equation (4)) and the temporal variation of the stress amplitude (given by the time histories of the bending forces $F_1$ and $F_2$). The determination of the average value and variance of the stress amplitude within the specimen gauge section thus involves evaluating equation (4) for the whole duration of the test. This can be done partly analytically by applying the calculation rules of variance and integrating equation (4) over the specimen gauge length, which results in the following equations for the average stress amplitude and its variance:

$$\tilde{\sigma}_a = mean(\tilde{\sigma}(x,t)) = mean\left(\overline{F}(t)\frac{a}{W_0}\right) = \frac{a}{W_0}mean\left(\overline{F}(t)\right) \tag{7}$$

$$var(\sigma_a(x,t)) = \left(\frac{a}{W_0}\right)^2 var\left(\overline{F}(t)\right) + \frac{1}{12}\left(\frac{aL_0}{W_0L}\right)^2 mean\left((\Delta F(t))^2\right) \tag{8}$$

As expected, the average stress amplitude depends only on the time-average of the mean bending force (equation (7)), whereas the variance of the stress amplitude given by equation (8) entails both the spatial and temporal variations described above.

The above-presented approach for the calculation of the stress amplitude variance is conservative, since equation (4) does not take into account the rotation of the specimen. That is, the variance given by equation (8) is in effect based on evaluating the stress amplitude on the scale of a given *specimen cross-section* (circumference), not on the scale of an *individual material point*. This fact is closely related to the possible geometrical imperfections of the specimen and will be discussed in detail below.

Figure 6 illustrates different kinds of specimen imperfections and their effect on the bending loads. Firstly, if the specimen is straight and rotationally symmetric, then the bending forces remain at a constant level when the main shaft rotates (Fig. 6(a)). In this case, the evaluation of the average stress amplitude and its variance (equations (7) and (8)) is almost trivial. However, if there is initial curvature in the specimen on a given plane (Fig. 6(b)), then an additional bending moment is applied to the specimen, as it is forced to align with the shafts. This results in the bending forces changing cyclically in the *same phase*; as the specimen rotates, the measured bending forces change depending on whether the initial curvature acts against or along the externally applied bending. On the other hand, if the specimen has an offset along its centerline on a given plane (Fig. 6(c)), then a gradient in the bending moment is generated along the specimen axis. This results in the bending forces changing cyclically in the *opposite phase*. In practice, both these idealized cases can take place simultaneously. Moreover, these imperfections may not necessarily share a common plane. However, both imperfections result in forces vibrating at the rotation frequency of the shaft. Therefore, it can be written:



**Fig. 6** Illustration of the effects of specimen imperfections on the measured bending loads during operation: (**a**) the rotationally symmetric straight specimen results in constant bending forces, (**b**) the initially curved specimen results in cyclically alternating bending forces at the same phase, and (**c**) a specimen with a centerline offset results in cyclically alternating bending forces at opposite phases
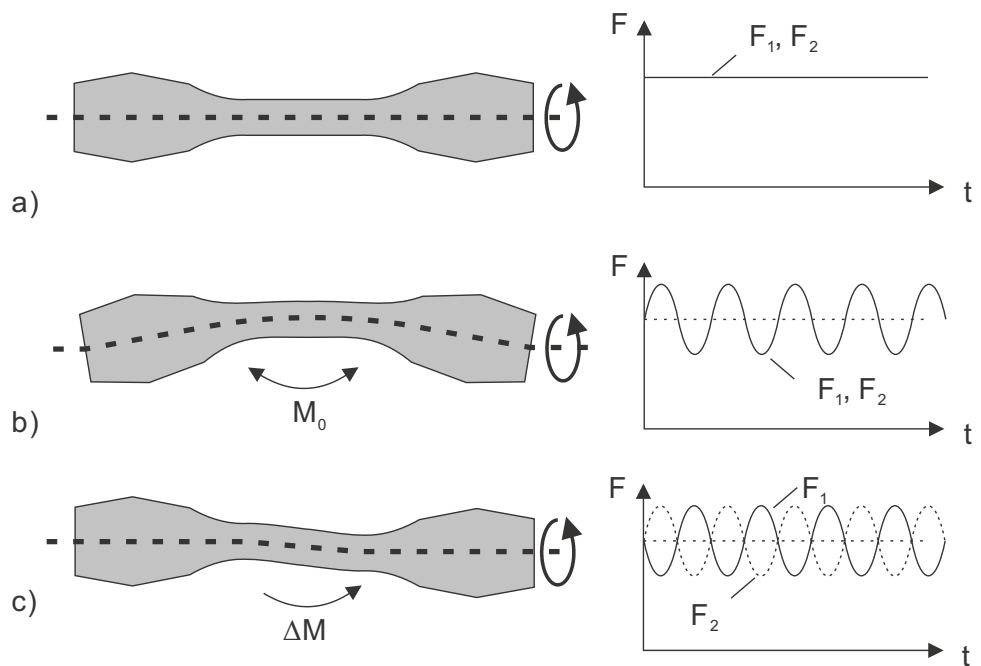
$$F_1(t) = \overline{F_1} + F_0\sin(2\pi ft + \varphi) - \widehat{F}\sin(2\pi ft) \tag{9}$$

$$F_2(t) = \overline{F_2} + F_0\sin(2\pi ft + \varphi) + \widehat{F}\sin(2\pi ft) \tag{10}$$

where $\overline{F_1}$ ja $\overline{F_2}$ denote the static bending forces (assumed constant), $F_0$ denotes the amplitude of the mean bending force resulting from the initial curvature of the specimen, and $\widehat{F}$ denotes the amplitude of the vibration caused by the centerline offset. The phase angle ($\varphi$) accounts for the above-discussed fact that the imperfections may not lie on the same plane. The unknowns in equations (9) and (10) can be solved separately by considering the average bending force and the difference between the forces:

$$\overline{F}(t) = \frac{1}{2}\left(F_1(t) + F_2(t)\right) = \frac{1}{2}\left(\overline{F_1} + \overline{F_2}\right) + F_0\sin(2\pi ft + \varphi) \tag{11}$$

$$\Delta F(t) = F_2(t) - F_1(t) = \overline{F_2} - \overline{F_1} + 2\widehat{F}\sin(2\pi ft) \tag{12}$$

As is evident in equations (11) and (12), a relatively straightforward fitting procedure can be applied to determine the constants of the above-presented model.

It should be noted that since the above-presented geometrical imperfections are fixed with respect to the specimen coordinate system, also the additional loading caused by these imperfections is fixed to the specimen, i.e., this loading appears as the static (spatially varying) *mean* load on specimen points superimposed on the cyclic loading.

Figure 7 presents an example of the data recorded during a test run at the maximum operating speed of 48 Hz (an example of a fractured test specimen is given in the Appendix). The strain gauge data shown in Fig. 7(a) indicate sinusoidal loading at a constant amplitude and frequency at a specific point (center) on the specimen surface. This is expected based on the basic operating principle of the device. In contrast, the measured bending forces (Fig. 7(b)), which should ideally be constant, fluctuate rather strongly in this case. Figure 7(c) shows the calculated bending stress amplitude distribution within the specimen gauge section (equation (4)) as a function of time. As can be seen, there is both spatial and temporal variation in the stress amplitude, i.e., there is a gradient in the stress amplitude along the longitudinal coordinate axis and a cyclic time-dependence of the mean stress amplitude. As discussed above, a conservative approach would entail calculating the mean and variance for the whole gauge section throughout the test using equations (7) and (8). For the data shown in Fig. 7, this approach leads to a relative standard deviation of 2.7%.

The bending force data can be further analyzed with the specimen model discussed above. Figure 7(d) shows the amplitude-frequency spectrum for both the mean bending force and for the difference of the bending forces (equations (5) and (6)). As can be seen, the assumptions made in equations (9) to (12) are well supported by the experimental data; the vibrations in the load data take place almost completely at the rotating frequency of the main shaft ($f$) with secondary peaks corresponding to synchronous components $(2, 3… * f)$. This results in the good fit of equations (11) and (12) to the experimental data, as shown by Figs. 7(e) and (f), respectively. The largest discrepancy between the measurement data and the model fit is seen in the case of the mean force (Fig. 7(e)). This discrepancy appears because the above-mentioned synchronous secondary vibration components were not included in the model. However, as seen in Fig. 7(e), the discrepancy is small (around 0.05 kN, whereas the force level is around 2.5 kN), and therefore the model accuracy is considered to be sufficient. Finally, a comparison of the model predictions with the experimentally measured bending forces (Fig. 7(b)) shows a good correspondence, that is, the assumptions made on the specimen imperfections and their effect on the measured loads (Fig. 6) are well supported by the experimental data. This conclusion is supported by additional experimental data measured at lower rotation speeds (not shown here), where the secondary vibration components are negligible.

Based on the above-presented analysis, the following can be concluded for the test data shown in Fig. 7: The initial curvature of the specimen (Fig. 6(b)) leads to an additional bending moment imposed on the specimen on one particular plane with a (maximum) relative value of 3.0% of the mean bending moment (calculated based on Fig. 7(e) and utilizing equation (4)). In addition, the initial offset in the specimen axis (Fig. 6(c)) results in a bending moment gradient within the specimen gauge section with a (maximum) relative value of 2.4% with respect to the mean bending moment (calculated based on Fig. 7(f) and utilizing equation (4)). As discussed above, these additional loads are fixed to the specimen coordinate system, i.e., they result in mean loading superimposed on the cyclic loading on individual specimen points. Thus, as a summary, the conservative analysis indicates a 2.7% relative standard deviation on the imposed cyclic loading amplitude. In contrast, the more detailed analysis based on relatively simple assumptions indicates that this deviation is largely explained by the geometrical imperfections of the specimen, which results in local mean stresses in individual specimen points. As presented above, this effect can be taken into account in the analysis of the test data. Furthermore, it has been observed that the amplitude of the synchronous vibration components (Fig. 7(d)) in the load signals can be reduced by operating the machine at a lower—but still sufficiently high—testing frequency of 20 Hz. This facilitates better measurement accuracy, when required. In the experiment presented above, the specimen stress amplitude was ~ 520 MPa, but similar conclusions apply also at considerably higher load amplitudes (so far, experiments have been carried out at 900 MPa).
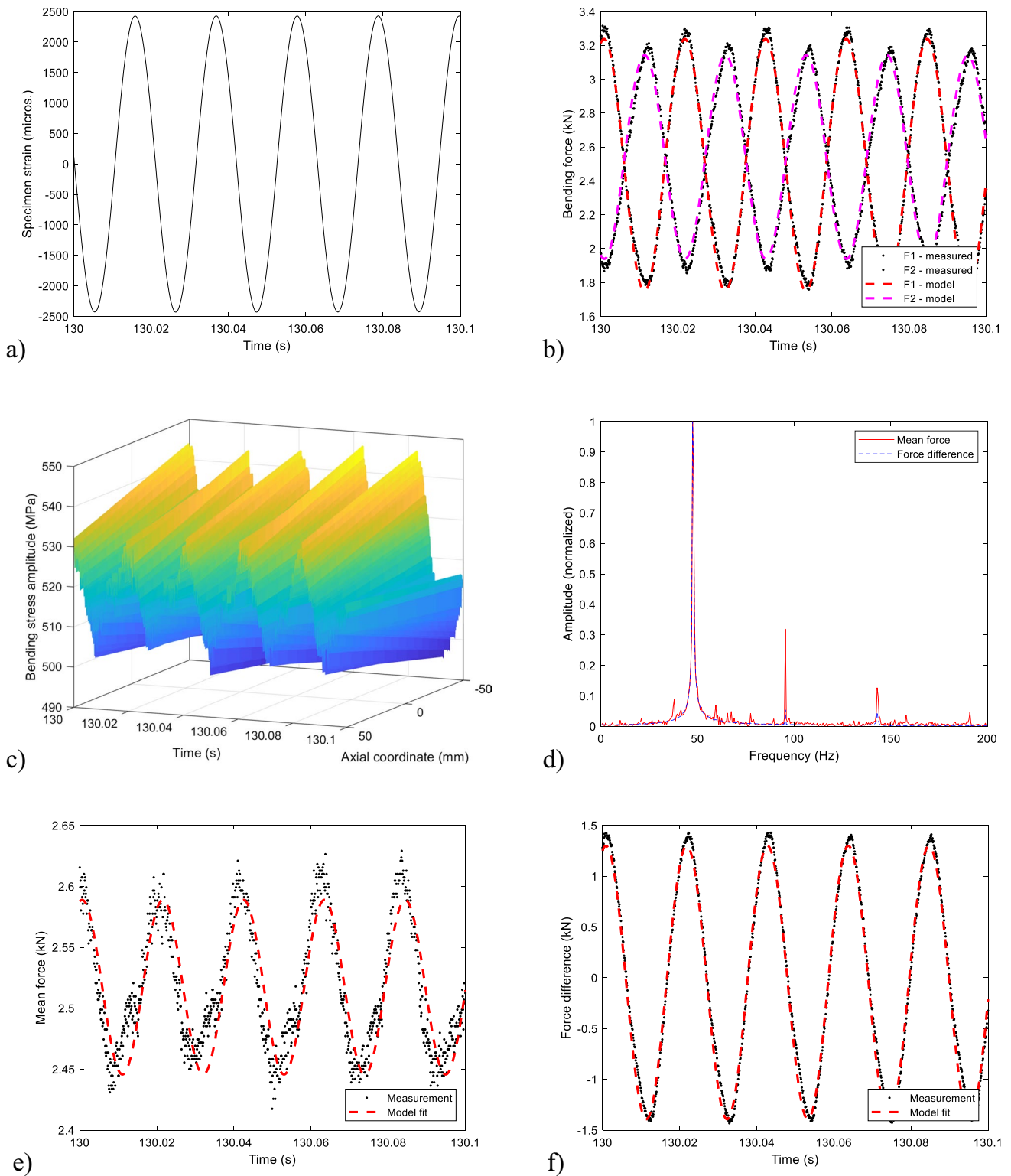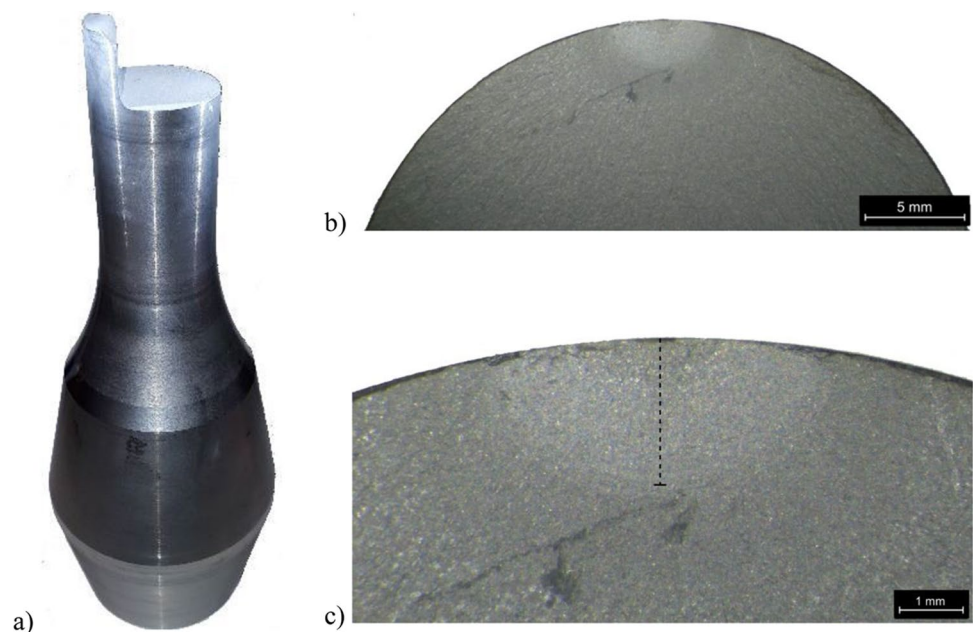
**Fig. 7** Example of the specimen loading in a fatigue test run at 48 Hz: (**a**) surface strain in the specimen center measured by the wireless strain gauge telemetry system, (**b**) bending forces measured by the load cells, (**c**) bending stress amplitude distribution within the specimen gauge section calculated directly based on the bending forces (equation (4)), (**d**) amplitude-frequency spectrum of the mean bending force and the difference of the bending forces, and (**e**) and (**f**) amplitude-time data of the mean bending force and difference of bending forces, respectively. The numerical fit described by equations (9) to (12) is shown in conjunction with the corresponding bending force data

## Conclusions

In this work, a large-scale fatigue testing machine based on the rotating beam method in a four-point bending configuration was developed. With the developed device, high-strength metal specimens with a gauge diameter of 32 mm and a gauge length of 100 mm can be tested at a cyclic frequency of up to 48 Hz. The main motivation for the work was to develop the capability for the measurement of fatigue properties of specimens with the size, microstructure, and surface conditions corresponding to actual machine parts. This capability enables the mitigation of the challenges of using data from small-scale laboratory specimens to predict the fatigue properties of large-scale components and structures. This is especially important in cases where some steps in the manufacturing process, such as heat treatments, introduce size dependency on the material fatigue properties.

This work presents a detailed account of the design and operational aspects of the developed test device. It is highlighted that in this kind of large-scale testing, careful attention must be paid to the uniformity of the applied loading in the specimen gauge section. Large specimens are prone to geometrical imperfections, which are challenging to remove completely during specimen preparation. These imperfections, when present, affect the uniformity of the loading in the specimen. Therefore, methods were developed to quantitatively evaluate both the spatial and temporal variations of the applied loading in the specimen based on the time-histories of the global bending forces.

## Appendix: Fatigue failure of the specimen

Figure 8 presents a typical example of a high-strength quenched and tempered steel specimen tested until failure. As can be seen, the fatigue crack nucleated at the surface of the specimen within the gauge length and then propagated ~ 2.5 mm before the final fracture took place practically within one loading cycle (this was verified by both the *in-situ* strain gauge and bending force data).

### Declarations

**Competing Interests** On behalf of all authors, the corresponding author states that there is no conflict of interest.

**Fig. 8** **a** Example of a fractured specimen, (**b**) and (**c**), example of a fatigue failure surface. In (**c**) the area of the stable fatigue crack propagation is highlighted by the vertical line

# References

1. Zhu SP, Ai Y, Liao D et al (2021) Recent advances on size effect in metal fatigue under defects: a review. Int J Fract. https://doi.org/10.1007/s10704-021-00526-x

2. Qian G, Lei W-S (2019) A statistical model of fatigue failure incorporating effects of specimen size and load amplitude on fatigue life. Phil Mag 99:2089–2125. https://doi.org/10.1080/14786435.2019.1609707

3. Rabb R (2013) Todennäköisyysteoriaan pohjautuva väsymisanalyysi. Wärtsilä Finland Oy, Vaasa. ISBN: 978–952–286–210–5

4. Wormsen A, Sjödin B, Härkegård G, Fjeldstad A (2007) Non-local stress approach for fatigue assessment based on weakest-link theory and statistics of extremes. Fatigue Fract Eng Mater Struct 30:1214–1227. https://doi.org/10.1111/J.1460-2695.2007.01190.X

5. El Haddad MH, Topper TH, Smith KN (1979) Prediction of non propagating cracks. Eng Fract Mech 11:573–584. https://doi.org/10.1016/0013-7944(79)90081-X

6. McEvily AJ, Endo M, Yamashita K, Ishihara S, Matsunaga H (2008) Fatigue notch sensitivity and the notch size effect. Int J Fatigue 30:2087–2093. https://doi.org/10.1016/j.ijfatigue.2008.07.001

7. Makkonen M (2003) Notch size effects in the fatigue limit of steel. Int J Fatigue 25:17–26. https://doi.org/10.1016/S0142-1123(02)00053-1

8. Härkegård G, Halleraker G (2010) Assessment of methods for prediction of notch and size effects at the fatigue limit based on test data by Böhm and Magin. Int J Fatigue 32:1701–1709. https://doi.org/10.1016/j.ijfatigue.2010.03.011

9. Shirani M, Härkegård G (2011) Fatigue life distribution and size effect in ductile cast iron for wind turbine components. Eng Fail Anal 18:12–24. https://doi.org/10.1016/j.engfailanal.2010.07.001

10. Beretta S, Ghidini A, Lombardo F (2005) Fracture mechanics and scale effects in the fatigue of railway axles. Eng Fract Mech 72:195–208. https://doi.org/10.1016/j.engfracmech.2003.12.011

11. Schneider S, Herrmann R, Marx S, Marx S (2018) Development of a resonant fatigue testing facility for large-scale beams in bending. Int J Fatigue 113:171–183. https://doi.org/10.1016/j.ijfatigue.2018.03.036

12. Weich I, Lorenz J, Fischl A, Rodic S, Buschner J (2012) Prüfungen im großen Maßstab. Stahlbau 81:203–211. https://doi.org/10.1002/stab.201201531

13. Varma AH, Russell BW, Wallace B (1997) Large-Scale Rotating Bending Fatigue Tests for Offshore Pipe Connections. Exp Mech 37:147–153. https://doi.org/10.1007/BF02317851

14. Toplack G (2008) Untersuchung des Grösseneinflusses auf Basis der Methode der Lokalen Spannungen anhand des Vergütungsstahles 34CrNiMo6, Dissertation, Montanuniversität Leoben, Austria

15. Bell K (2017) Full-Scale Testing of the Fatigue Life of Laser Additive Manufacturing Repaired Alloy Steel Components, Master of Science Thesis, Department of Chemical and Materials Engineering University of Alberta

16. Shirani M, Härkegård G (2011) Large scale axial fatigue testing of ductile cast iron for heavy section wind turbine components. Eng Fail Anal 18:1496–1510. https://doi.org/10.1016/j.engfailanal.2011.05.005

17. Ulrich KT, Eppinger SD (2012) Product Design and Development, 5th edn. McGraw-Hill Education, New York (ISBN: 978-007-340-477-6)

18. Wright IC (1998) Design Methods in Engineering and Product Design. McGraw-Hill, London (ISBN: 978-007-709-376-1)

19. ISO 1143:2010 (2010) Metallic materials — Rotating bar bending fatigue testing. International Organization for Standardization, 26 p

20. Hills DA, Nowell D (1994) Mechanics of Fretting Fatigue. Springer Science+Business Media, Dordrecht (ISBN: 978-94-015-8281-0)

21. Hintikka J, Mäntylä A, Vaara J, Frondelius T, Lehtovaara A (2019) Stable and unstable friction in fretting contacts. Tribol Int 131:73–82. https://doi.org/10.1016/j.triboint.2018.10.014

22. Juoksukangas J, Lehtovaara A, Mäntylä A (2016) Experimental and numerical investigation of fretting fatigue behavior in bolted joints. Tribol Int 103:440–448. https://doi.org/10.1016/j.triboint.2016.07.021